

A universal resist-assisted metal transfer method for 2D semiconductor contacts

Xuanye Liu(刘轩冶), Linxuan Li(李林璇), Chijun Wei(尉驰俊), Peng Song(宋鹏), Hui Gao(高辉), Kang Wu(吴康), Nuertai Jiazila(努尔泰·加孜拉), Jiequn Sun(孙杰群), Hui Guo(郭辉), Haitao Yang(杨海涛), Wu Zhou(周武), Lihong Bao(鲍丽宏), and Hong-Jun Gao(高鸿钧)
Citation: Chin. Phys. B, 2024, 33 (**12**): 127302. DOI: 10.1088/1674-1056/ad8db4
Journal homepage: http://cpb.iphy.ac.cn; http://iopscience.iop.org/cpb

What follows is a list of articles you may be interested in

Anomalous valley Hall effect in two-dimensional valleytronic materials

Hongxin Chen(陈洪欣), Xiaobo Yuan(原晓波), and Junfeng Ren(任俊峰)
Chin. Phys. B, 2024, 33 (**4**): 047304. DOI: 10.1088/1674-1056/ad1c59

Hexagonal boron phosphide and boron arsenide van der Waals heterostructure as high-efficiency solar cell

Yi Li(李依), Dong Wei(魏东), Gaofu Guo(郭高甫), Gao Zhao(赵高), Yanan Tang(唐亚楠), and Xianqi Dai(戴宪起)
Chin. Phys. B, 2022, 31 (**9**): 097301. DOI: 10.1088/1674-1056/ac6b2a

Digital and analog memory devices based on 2D layered MPS_3 (M=Mn, Co, Ni) materials

Guihua Zhao(赵贵华), Li Wang(王力), Xi Ke(柯曦), and Zhiyi Yu(虞志益)
Chin. Phys. B, 2021, 30 (**4**): 047303. DOI: 10.1088/1674-1056/abd397

Recent progress on the prediction of two-dimensional materials using CALYPSO

Cheng Tang(唐程), Gurpreet Kour, Aijun Du(杜爱军)
Chin. Phys. B, 2019, 28 (**10**): 107306. DOI: 10.1088/1674-1056/ab41ea

Electronic and magnetic properties of CrI_3 nanoribbons and nanotubes

Ji-Zhang Wang(王吉章), Jian-Qi Huang(黄建啟), Ya-Ning Wang(王雅宁), Teng Yang(杨腾), Zhi-Dong Zhang(张志东)
Chin. Phys. B, 2019, 28 (**7**): 077301. DOI: 10.1088/1674-1056/28/7/077301

SPECIAL TOPIC — Stephen J. Pennycook: A research life in atomic-resolution STEM and EELS

A universal resist-assisted metal transfer method for 2D semiconductor contacts

Xuanye Liu(刘轩冶)[1,2,†], Linxuan Li(李林璇)[2,†], Chijun Wei(尉驰俊)[2], Peng Song(宋鹏)[1,2], Hui Gao(高辉)[1,2], Kang Wu(吴康)[1,2], Nuertai Jiazila(努尔泰·加孜拉)[1,2], Jiequn Sun(孙杰群)[1,2], Hui Guo(郭辉)[1,2,3], Haitao Yang(杨海涛)[1,2,3], Wu Zhou(周武)[2,‡], Lihong Bao(鲍丽宏)[1,2,3,§], and Hong-Jun Gao(高鸿钧)[1,2,3]

[1] *Institute of physics, Chinese Academy of Sciences, Beijing* 100190, *China*
[2] *School of Physical Sciences, University of Chinese Academy of Sciences, Beijing* 100049, *China*
[3] *Hefei National Laboratory, Hefei* 230088, *China*

(Received 26 September 2024; revised manuscript received 31 October 2024; accepted manuscript online 1 November 2024)

With the explosive exploration of two-dimensional (2D) semiconductors for device applications, ensuring effective electrical contacts has become critical for optimizing device performance. Here, we demonstrate a universal resist-assisted metal transfer method for creating nearly free-standing metal electrodes on the SiO_2/Si substrate, which can be easily transferred onto 2D semiconductors to form van der Waals (vdW) contacts. In this method, polymethyl methacrylate (PMMA) serves both as an electron resist for electrode patterning and as a sacrificial layer. Contacted with our transferred electrodes, MoS_2 exhibits tunable Schottky barrier heights and a transition from n-type dominated to ambipolar conduction with increasing metal work functions, while InSe shows pronounced ambipolarity. Additionally, using α-In_2Se_3 as an example, we demonstrate that our transferred electrodes enhance resistance switching in ferroelectric memristors. Finally, the universality of our method is evidenced by the successful transfer of various metals with different adhesion forces and complex patterns.

Keywords: metal electrode transfer, 2D materials, Schottky barrier, ambipolar, memristor

PACS: 73.40.Ns, 72.20.Fr, 73.30.+y, 73.20.–r **DOI:** 10.1088/1674-1056/ad8db4

1. Introduction

Two-dimensional (2D) layered materials have atomic thickness and are free of dangling bonds, therefore, they are expected to break through the bottleneck of traditional Si-based circuits and further extend Moore's law.[1–4] Among these materials, transition metal dichalcogenides (TMDs) and Ⅲ–Ⅵ group compound semiconductors, such as MoS_2[5] and InSe,[6] have been extensively studied and utilized in electronic and optoelectronic devices.[7–10] Particularly, α-In_2Se_3, which combines semiconductor properties with ferroelectricity even down to the monolayer,[11–13] has been widely used in memristors to emulate biological synaptic behaviors and applied to in-memory computing.[14–18] However, the performance of these 2D semiconductor devices is severely limited by poor metal–semiconductor contacts fabricated using conventional aggressive lithography and deposition processes,[19–22] in which the introduction of defects and penetration at the metal–semiconductor interfaces inevitably occur, leading to strong Fermi-level pinning (FLP) and unintended doping of the channel.[23,24]

To enhance the device performance, various contact strategies have been developed, such as heavily doping the contact areas to narrow the barrier width,[25] phase engineering to semi-metalize (yttrium-doped InSe[6]) or metalize (1T-MoS_2[26,27]) the contact region of the channel, and using semimetal electrodes to suppress the metal-induced gap states (bismuth[28]) or hybridize the metal–semiconductor energy bands (antimony $(01\bar{1}2)$[29]). Additionally, vdW contacts formed by transferred electrodes have been developed.[22–24,30–35] In this approach, the metal electrodes are pre-deposited on the substrate and then physically laminated onto 2D semiconductors, creating a vdW gap between the metal electrodes and 2D semiconductor channels, leading to the formation of atomically sharp contact interfaces that preserve the inherent properties of the 2D semiconductors.[22,36] However, several challenges remain with this approach. For instance, the strong adhesion force between pre-deposited metal electrodes and the substrate hinders the final pick-up of the metal electrodes.[23,30,34] Although various routes have been proposed and excellent contact performance has been achieved so far, the methods still have limitations.[36] For example, to facilitate the pick-up of metal electrodes, toxic hexamethyldisilazane (HMDS) is used to functionalize the silicon wafer, but the transfer yields remain low for metals with strong adhesion forces;[22] special substrates like CVD-grown graphene on Ge wafer[30] or freshly cleaved F-mica[23] are uti-

[†]These authors contributed equally to this work.
[‡]Corresponding author. E-mail: wuzhou@ucas.ac.cn
[§]Corresponding author. E-mail: lhbao@iphy.ac.cn

© 2024 Chinese Physical Society and IOP Publishing Ltd

lized to reduce the adhesion force, while these substrates can increase complexity compared to currently mature Si-based process. Other methods, such as picking up the electrodes embedded in hBN flakes[24] or adhered to ZnO nanobelts,[34] not only involve elaborate electrode fabrication processes but also constrain the size and patterns of electrodes by the shapes of the exfoliated hBN flakes or CVD-grown ZnO nanobelts. Developing a universal and efficient method for fabricating transfer electrodes is highly desired.

Here, we developed a universal resist-assisted transfer method to transfer nearly free-standing metal electrodes onto 2D semiconductors, thereby avoiding the adhesion forces between the metal and substrate. In this method, spin-coated PMMA layer serves both as electron resist for defining electrode patterns through electron-beam lithography (EBL) and as a sacrificial layer for metal deposition, resulting in nearly free-standing metal electrodes after PMMA dissolution. As a result, the adhesion between the metal electrodes and the SiO_2/Si substrate can be prevented. We applied this method to fabricate MoS_2 and InSe field-effect transistors (FETs) on hBN substrates with different contacted metals, achieving atomically uniform channels for MoS_2 without damage, as confirmed by scanning transmission electron microscopy (STEM). With increasing metal work functions of the transferred electrodes (Ti, Cr, Au, Pd, and Pt), MoS_2 FETs show linearly increasing Schottky barrier heights (SBHs) with an extracted ideality factor (S) of ∼0.5 accompanied by a transition in transport behavior from n-type dominance to ambipolar. The InSe FETs perform a pronounced ambipolarity regardless of whether the contact metal has a low (Cr) or high (Pd) work function. Additionally, α-In_2Se_3 ferroelectric memristors show significantly enhanced ferroelectric resistance switching (FRS) with transferred electrodes compared to evaporated ones, due to the lack of screening of gap states. Finally, the universality of our methods is confirmed by picking up metals with different adhesion forces onto polypropylene carbonate (PPC) and transferring irregular-shaped patterns. Our method offers a versatile, efficient, and cost-effective approach for fabricating high-performance 2D semiconductor devices and complex metal microstructures.

2. Results and discussion

2.1. Fabrication and transfer process of metal electrodes

The fabrication and transfer process of the metal electrodes are schematically illustrated in Fig. 1(a). After the PMMA is spin-coated onto the SiO_2/Si substrate (i), the PMMA patterns are defined by a standard EBL process (ii). Notably, some micro-patterns form at the PMMA corners as shown in the enlarged view of step (ii). This is followed by electron-beam metal deposition (iii), where metallic "micro-joints" at the corners of the "electrode" pattern are created based on the shape of the micro-patterns on PMMA. After soaking in acetone and isopropanol, the remaining patterned PMMA, acting as a sacrificial layer, is removed, leaving nearly free-standing metal electrodes weakly connected to an external frame via the micro-joints (iv). Due to the weak connection between the electrode and frame, the patterned metal electrodes can be easily picked up using PDMS/PPC adhesive tape (v) and then laminated onto the mechanically exfoliated MoS_2 flake on the SiO_2/Si substrate (vi). By heating the substrate to 95 °C, the metal electrodes with the PPC film are released onto the MoS_2 channel (vii), completing the device fabrication. An optical image of the device is shown in Fig. 1(b), where the remaining PPC capping protects the device from H_2O/O_2 degradation. Furthermore, as shown in Fig. 1(c), the PPC capping can also be removed after sequentially soaking in acetone and isopropanol (viii). The optical images of the above steps are shown in Fig. S1. Additionally, to fabricate the device on flexible PPC film, the MoS_2 channel on the SiO_2/Si substrate can also be transferred onto the electrodes on the PDMS/PPC tape (ix). Figure 1(d) shows an optical image of an hBN-capped MoS_2 device on PPC film, with the detailed fabrication process illustrated in Fig. S2.

Overall, there are two crucial points in our method. The first is the nearly free-standing electrodes fabricated by dissolving the underlying PMMA sacrificial layer, which ensures that the electrode pick-up process is independent of the adhesion force between the metal electrode and the SiO_2/Si substrate. The second is the introduction of micro-joints, which weakly connect the "electrode" and "frame" regions and effectively prevent the detachment of the electrodes from the SiO_2/Si substrate. The detailed fabrication process and important role of micro-joints are shown in Figs. S3–S6.

2.2. MoS_2 and InSe FETs contacted with transferred metal electrodes

To show the superiority and universality of our metal transfer method, field-effect transistors with contact metals of different work functions were fabricated, including Ti (∼4.3 eV), Cr (∼4.6 eV), Au (∼4.8 eV), Pd (5.1 eV), and Pt (∼5.6 eV). As an example, we used few-layer MoS_2 as the channel material. The structure and optical image of the device are illustrated in Fig. 2(a), where few-layer hBN severs as an atomically flat substrate to mitigate carrier scattering and charge trapping at the SiO_2 interface.[37] These metal work functions span the range from the conduction band (E_{CB}) to valence band (E_{VB}) of few-layer MoS_2,[38] and the energy band diagram of the MoS_2 channel and metals before contact is illustrated in Fig. 2(b).

Aberration-corrected STEM was conducted to characterize the interface properties between MoS_2 and the transferred metal electrodes. As shown in the cross-sectional high-angle

annular dark-field (HAADF) STEM image in Fig. 2(c), a ~2 nm gap is observed between the Ti electrode and the MoS_2 channel. The elemental mapping via electron energy loss spectroscopy (EELS) shown in Fig. 2(d) reveals prominent carbon signals in this region, which is attributed to organic residues (originating from the PMMA sacrificial layer). To eliminate the influence of organic residues on the electrical properties of MoS_2 FETs, we utilize reactive ion etching (RIE) to remove the residues before laminating the electrodes onto the channel (Fig. S7). As shown in Fig. 2(e), after RIE treatment, the Ti lattices are partially in contact with the top layer of MoS_2 at the interface, suggesting direct contact between the metal electrode and MoS_2. In addition, the carbon signals in the gap are significantly reduced (Fig. 2(f)). Notably, for the devices with transferred electrodes, the MoS_2 channels remain uniform and free from penetrations or disorder (Fig. S8), regardless of whether the electrodes have been treated with RIE.

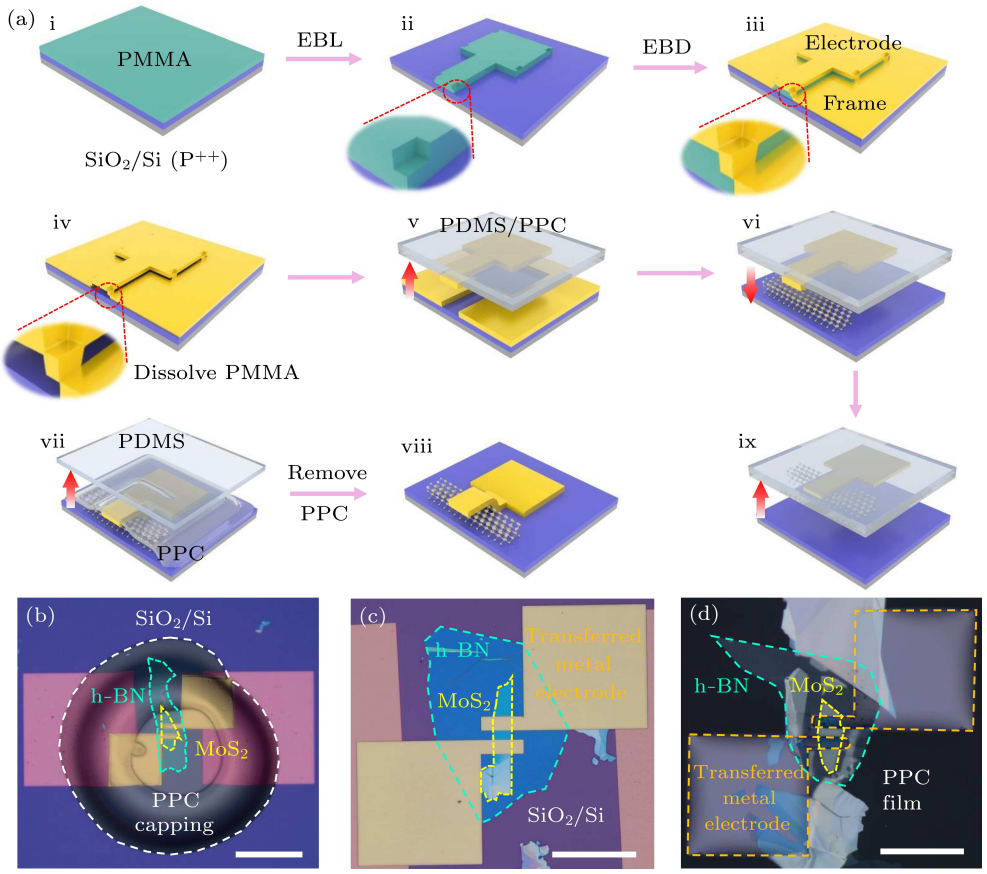


Fig. 1. Schematic illustration of the electrode fabrication and transfer processes. (a) i. PMMA was spin-coated onto the SiO_2/Si substrate; ii. Electrode patterns of electrode were defined by e-beam lithography; iii. The metal film was deposited by electron-beam deposition; iv. The sacrificial PMMA layer under the electrode was removed; v. The metal electrode was picked up by placing PDMS/PPC adhesive tape; vi. The metal electrode was aligned and physically laminated onto the MoS_2 channel on the SiO_2/Si substrate; vii. By heating the substrate, the PPC/electrode was released onto the MoS_2 channel; viii. The PPC capping was removed by sequentially soaking the substrate in acetone and isopropanol; ix. The MoS_2 channel was picked up onto the metal electrode on the PPC film, without heating the substrate. Optical image of (b) the fabricated PPC-capped MoS_2 transistor on the SiO_2/Si substrate, (c) MoS_2 transistor on the SiO_2/Si substrate after PPC removal, and (d) hBN-capped MoS_2 device on flexible PPC film. The scale bars are 75 μm for (b), and 50 μm for (c) and (d).

The transfer characteristics were measured by sweeping the gate voltage V_{GS} from −60 V to +60 V at $V_{DS} = 0.1$ V. Unlike MoS_2 FETs with evaporated electrodes (Fig. 2(g)), MoS_2 FETs with RIE-treated transferred electrodes (Fig. 2(h)) exhibit a transition from n-type to ambipolar transport behavior as the contact metals change from Cr to Pt with increasing work function. This transition suggests the Fermi-level de-pinning of the MoS_2 channel. We also compare the output characteristics of MoS_2 FETs with evaporated and RIE-treated transferred electrodes, as shown in Fig. S9. The increased non-linearity for electrodes after RIE treatment further confirms our speculations. Furthermore, as shown in Fig. S10, our devices also exhibit a subthreshold swing of ~495 mV/dec (for Pd) and a higher field-effect carrier mobility of ~320 $cm^2 \cdot V^{-1} \cdot s^{-1}$ (for Au) compared to previous works.[39]

To extract the effective SBH using the standard Arrhenius plot, variable-temperature electrical transport measurements on MoS_2 FETs with evaporated and transferred metal electrodes without and with RIE treatment were conducted (Fig. S11–13 and supplementary Note 2). The extracted electron barrier heights for different metal work functions are sum-

marized in Fig. 2(i). Due to the strong FLP, the barrier heights for evaporated electrodes (black square dots) do not exhibit apparent dependence on the work function, which is consistent with previous results.[22] For the directly transferred electrodes without RIE treatment (red circular dots and the red linear fitted line), the data exhibits a linear relationship with a slope (S) of ∼0.22, which can be attributed to the weakened modulation capability of the metal contact due to the presence of the organic gap. For the RIE treated transferred electrodes (blue triangle dots and the blue linearly fitted line), the electron barrier heights show significant modulation by the work function with a slop of ∼0.5, indicating the successful suppression of FLP, which highlights the significance of RIE treatment in the transfer method.

In addition to MoS_2, we also fabricated few-layer InSe FETs, with the device structure and energy band diagram illustrated in Figs. 3(a) and 3(b), respectively. It should be noted that all electrodes in subsequent experiments were transferred after RIE treatment. As shown in Figs. 3(d)–3(f), the transfer curves of InSe FETs with Cr, Au, and Pd contacts all exhibit ambipolar characteristics. From the transfer curves in the linear scale, we can observe that when changing contact metals from Cr to Pd with increasing work functions, the currents of the p-type branch gradually increase and surpass that of the n-type branch due to the rise (fall) of electron (hole) SBH. The transfer curves under different gate voltages are shown in Fig. S14. The observed ambipolar behavior arises not only from the defect states induced by selenium vacancy,[40] but also from the absence of FLP. As illustrated in Fig. 3(c), the Fermi level position can be tuned under different polarities of gate voltages, resulting in a change in the dominant carrier type (hole for $V_{GS} < 0$ and electron for $V_{GS} > 0$). Notably, the ambipolarity in InSe FETs, even with Cr contacts, is rarely reported before, as InSe typically exhibits electron-dominated characteristics[37,40] or ambipolarity when contacted with high work function metals.[33] Overall, due to the absence of FLP and intact channel, our InSe FETs exhibit intrinsic transport properties with pronounced ambipolarity, which enables applications in electrical[9] or optical[33,41] devices.

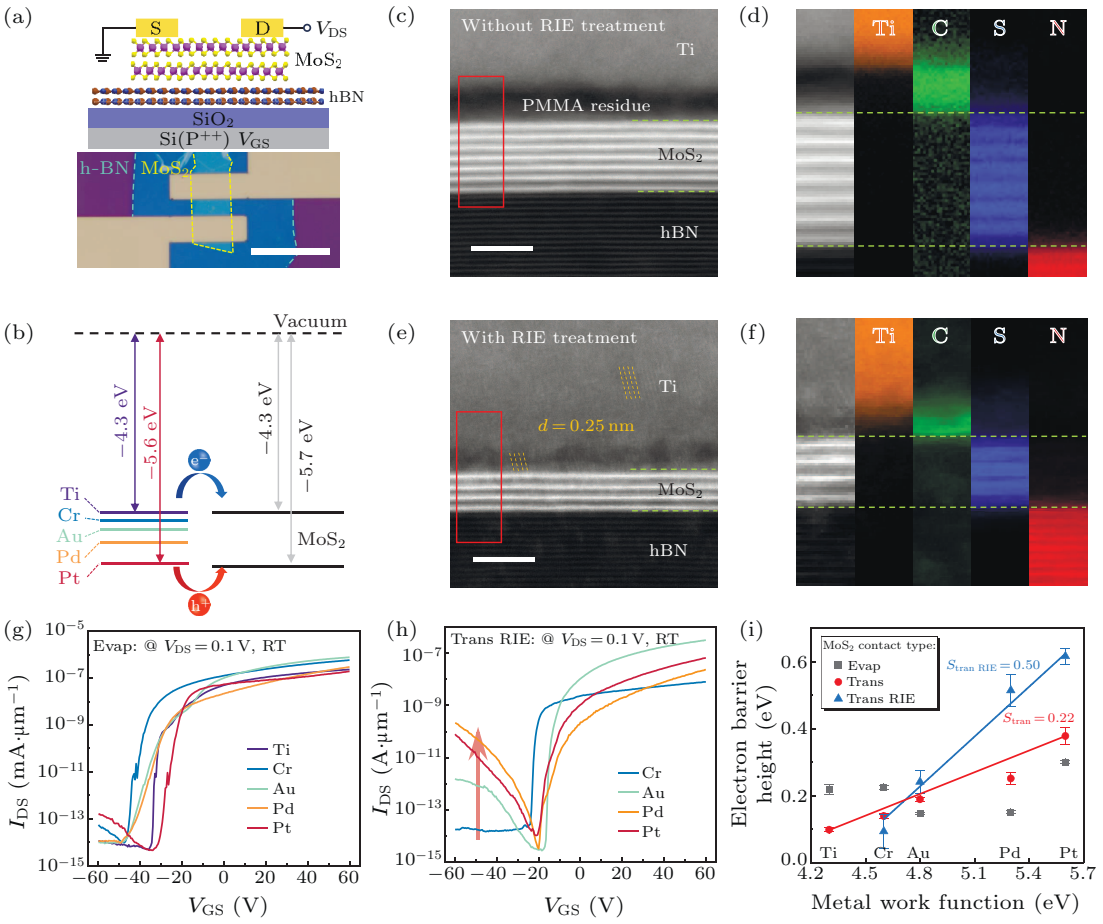


Fig. 2. Electrical characterization of MoS_2 FETs with transferred electrodes. (a) Schematic of a MoS_2 FET with transferred metal electrodes. An optical image is shown at the bottom. (b) Band diagram of multilayer MoS_2 and work functions of Ti, Cr, Au, Pd, and Pt, in equilibrium before contact. (c) STEM-HAADF and (d) EELS mapping images of the cross-section of the MoS_2 FET contacted by transferred Ti electrodes without RIE treatment. (e) STEM-HAADF and (f) EELS mapping images of the cross-section of the MoS_2 FET contacted by RIE-treated transferred Ti electrodes. (g) I_{DS}–V_{GS} transfer curves of MoS_2 FETs with evaporated electrodes. (h) I_{DS}–V_{GS} transfer curves of MoS_2 FETs with RIE-treated transferred metal electrodes. (i) Extracted electron Schottky barrier height (SBH) for different evaporated and transferred metals. The extracted ideality factors S for transferred electrodes without and with RIE treatment are 0.22 and 0.5, respectively. The scale bar is 25 μm for (a), 4 nm for (c) and (e).

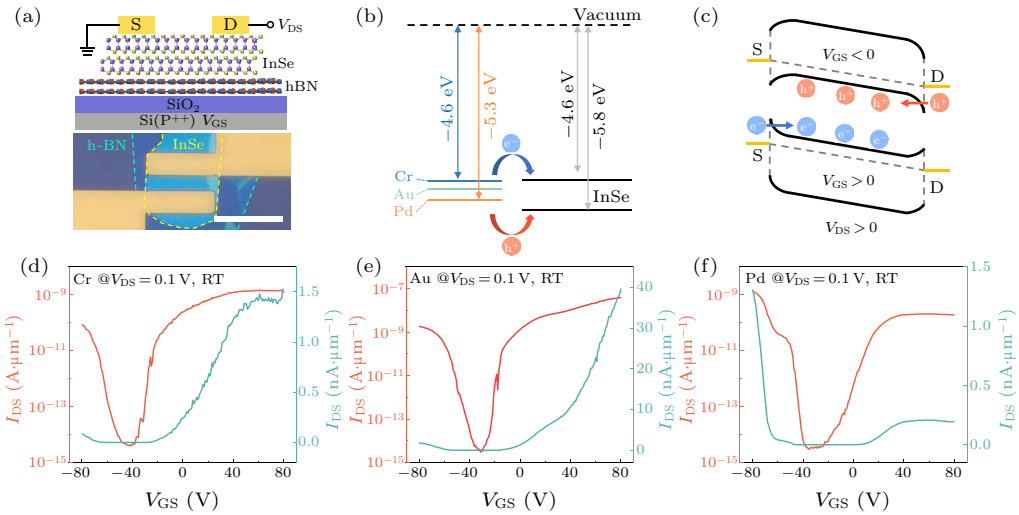


Fig. 3. Electrical characterization of InSe FETs with transferred electrodes. (a) Schematic of an InSe FET with transferred metal electrodes. An optical image is also shown at bottom. (b) Band diagram of multilayer InSe and work functions of Cr, Au, and Pd, in equilibrium before contact. (c) Energy band schematic of InSe FET under negative and positive gate voltages at $V_{DS} > 0$ V. The red balls represent hole carriers, and the blue balls represent electron carriers. I_{DS}–V_{GS} transfer curves of InSe FETs with transferred (d) Cr, (e) Au, and (f) Pd electrodes. Red curves are logarithmic; green curves are linear. The scale bar is 25 μm for (a).

2.3. Ferroelectric memristors contacted with transferred metal electrodes

The α-In_2Se_3, a recently identified ferroelectric semiconductor, is utilized as the channel material for ferroelectric memristors.[14,15,17,18,42,43] Their FRS regime in these devices is determined by ferroelectric polarization, SBH changes, and the initial barrier height.[44] Conventional contacts, however, often induce FLP, adversely affecting these factors and degrading the FRS performance. For the first time, we propose utilizing transferred metal electrodes to optimize the memristor contact, thereby enhancing the FRS.

Initially, we fabricated Au-contacted α-In_2Se_3 ferroelectric memristors with electrodes evaporated by electron-beam deposition method. Figures 4(a) and 4(b) present the dual-sweep output curves of the Au-contacted In_2Se_3 memristor under different drain bias voltages. For the small bias range (−0.5 V to +0.5 V, Fig. 4(a)), as the applied lateral electric field (∼0.1 V/μm) is below the in-plane coercive field of α-In_2Se_3 (E_C∼0.4 V/μm for our device), the polarization remains unswitched, resulting in negligible hysteresis. The strong non-linear behavior is indicative of an initial Schottky barrier. In contrast, at larger biases (−6 V to +6 V, Fig. 4(b)), which exceeds the in-plane coercive electric field of α-In_2Se_3, the hysteresis windows are significantly pinched, as similarly observed in another device (Fig. S15). This can be explained by the schematic diagram shown in Fig. 4(c). For a metal–semiconductor–metal device with a fixed bias (e.g., $V_{DS,\,read} > 0$), we can simplify its two-Schottky-barrier model to a single barrier model at the electron injection terminal (source terminal, supplementary Note 3).[45] Usually, FRS is attributed to the change of SBH modulated by switched polarization charges (supplementary Note 4). However, for the devices contacted with conventionally evaporated electrodes, the existence of high-density gap states can screen the polarization charges and constrain the SBH modulation, leading to negligible FRS.

To eliminate the effects of gap states, we fabricated α-In_2Se_3 ferroelectric memristors with transferred Au electrodes. As shown in Fig. 4(d), the output curves under small bias range still show an absence of a hysteresis window, but the near-linear behavior suggests the formation of Ohmic contact. Upon increasing the V_{DS} sweeping range, devices with transferred Au contacts exhibit gradually enlarging hysteresis windows (Fig. 4(e)) and significantly higher channel currents compared to their evaporated counterparts. Under sufficiently large V_{DS} and V_G ranges, both dual-sweep output curves and transfer curves show saturated hysteresis windows due to full in-plane and our-ot-plane polarization switching (Fig. S16), confirming that the observed FRS originates from ferroelectric polarization switching. We also fabricated α-In_2Se_3 ferroelectric memristors contacted with transferred Ti and Pt electrodes. The electrical characteristics are shown in Fig. S17. The different non-linearities of the output curves under a small bias range indicate varying initial SBH. All of them exhibit gradually enlarged and then saturated dual-sweep hysteresis windows in output and transfer curves. As the band diagram shown in Fig. 4(f), when the in-plane polarization of the channel is switched by positive or negative V_{DS} voltage, the absence of gap state screening allows effective SBH modulation by polarization charges, significantly altering the device resistance.

Our transfer electrode method markedly enhances the FRS of α-In_2Se_3 memristors, achieving more than an order of magnitude improvement in our devices. This novel interfacial engineering approach can also be extended to other thermionic emission dominated 2D long-channel memristors, showcasing its versatility and effectiveness.

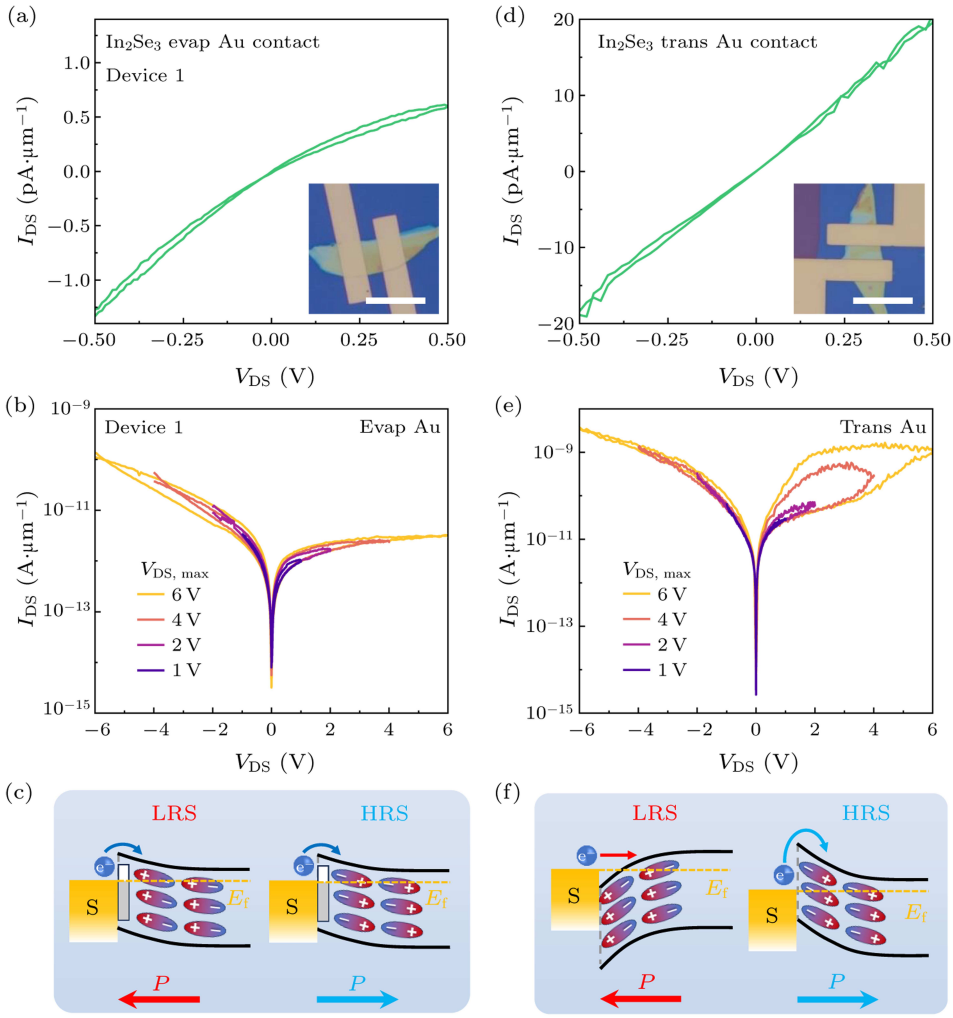


Fig. 4. Comparison of electrical performance of ferroelectric α-In_2Se_3 memristors with evaporated and transferred electrodes. (a), (d) I_{DS}–V_{DS} dual-sweep output curves of evaporated (a) and transferred (d) Au-contacted α-In_2Se_3 memristors under small V_{DS} sweeping range. The optical images of the devices are shown in the corners; scale bars are 20 μm. (b), (e) I_{DS}–V_{DS} dual-sweep curves of evaporated (b) and transferred (e) Au-contacted α-In_2Se_3 memristors under increasing V_{DS} sweeping range. (c), (f) Energy band diagrams at the electron injection side ($V_{DS} > 0$) of memristors with (c) evaporated electrodes and (f) transferred electrodes. The ellipses in the semiconductor band gap represent the in-plane ferroelectric dipoles in α-In_2Se_3 channel. The red and blue arrows indicate different polarization directions. The blue balls represent electrons. The gray rectangles between electrodes and channels indicate gap states.

2.4. Transferring metal with arbitrary types and patterns

Our transfer method is uniquely versatile, allowing the use of various metals regardless of the adhesion force between the metal and the substrate. For Au and Pt with weak adhesion force, Pd with intermediate adhesion force, and Ti and Cr with strong adhesion force,[22,30] 10×10 metal squares with a side length of 15 μm were fabricated and could all be successfully transferred onto PPC films with a yield of 100%, as shown in Figs. 5(a)–5(e). In addition to metal types, our method's compatibility with complex metal patterns further demonstrates its universality. To test this, we prefabricated a Hall bar pattern with six electrodes fixed by a surrounding frame on a SiO_2/Si substrate (Fig. 5(f)). This pattern was successfully transferred onto PPC tape, leaving the frame on the substrate (Fig. 5(g)), and then laminated onto a target 2D material without deformation (Fig. 5(h)). Furthermore, we verified the method's capability to transfer intricate irregular-shaped metal patterns. As an example, we pre-fabricated the "IOP" logo on a SiO_2/Si substrate (Fig. 5(i)), which was then picked up by PPC tape, leaving the complementary logo frame on the SiO_2/Si substrate (Fig. 5(j)). Finally, the IOP logo was laminated onto another substrate without any wrinkles (Fig. 5(k)).

We summarize the existing electrode transfer methods and compare them with our approach in Table S1 and supplementary Note 6. While previous methods have achieved notable contact performance, such as approaching the Schottky–Mott limit for MoS_2/PMMA[22] and WSe_2/PMMA FETs,[34] p-type bilayer WSe_2 FET with high hole mobility and low contact resistance,[24] and ultra-stable t-Au/graphene contact under harsh environments,[31] etc., they often suffer from limitations.[36] For example, low transfer yields for strong-adhesion metals, the need for additional materials or special substrates to weaken the adhesion force, and restrictions on the metal pattern design, all of which increase complexity.

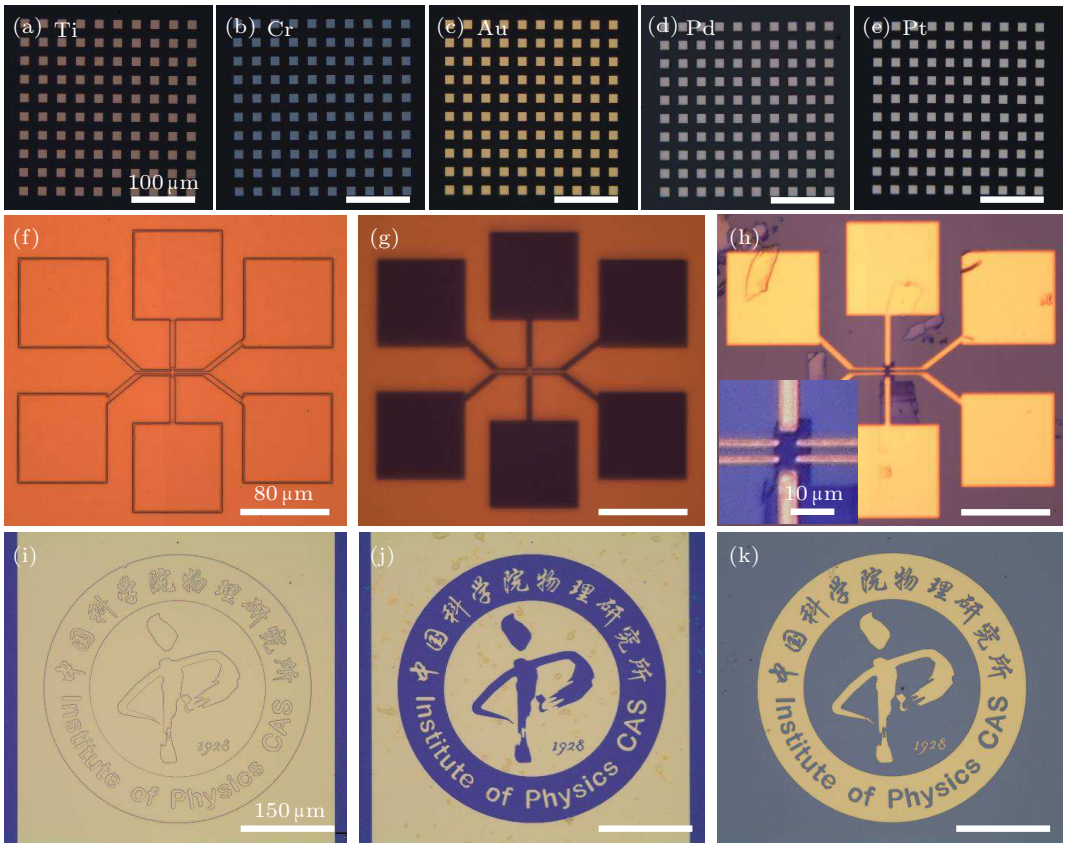


Fig. 5. Universality of the metal transfer method. Optical images of 10×10 metal squares on PDMS/PPC tapes with 100% transfer yields, for (a) Ti, (b) Cr, (c) Au, (d) Pd, and (e) Pt. Optical images of fabricated Hall bar electrodes on the SiO_2/Si substrate (f), the surrounding frame remaining on the SiO_2/Si substrate (g), and the Hall bar transferred onto the target 2D material on another SiO_2/Si substrate (h). The left corner of (h) shows a zoomed-in optical image of the center contact region of the Hall bar device, with an electrode width of 1 μm. Optical images of fabricated IOP logo on the SiO_2/Si substrate (i), the complementary frame remaining on the SiO_2/Si substrate (j), and the IOP logo transferred onto another SiO_2/Si substrate (k). The scale bars are 100 μm for (a)–(e), 80 μm for (f)–(h), 150 μm for (i)–(k), and 10 μm for the zoomed-in optical image in (h).

In contrast, our metal prefabrication process uses straightforward lithography and metal deposition on traditional silicon wafers, and the resulting freestanding metal film eliminates peeling issues, making it suitable for a wide range of metals and patterns.

3. Conclusion

In summary, we have developed a universal resist-assisted method for transferring electrodes to contact with 2D semiconductors. This method employs PMMA as a sacrificial layer and introduces metallic "micro-joints" to create nearly freestanding electrodes on the SiO_2/Si substrate, which can be easily picked up. 2D semiconductor FETs fabricated by our transfer method feature atomically uniform channels and exhibit intrinsic transport properties. With increasing metal work functions of transferred electrodes (Ti, Cr, Au, Pd, and Pt), MoS_2 FETs show linearly increasing Schottky barrier heights accompanied by a transition in transport behavior from n-type dominated to ambipolar. All InSe FETs exhibit pronounced ambipolarity. Additionally, the transferred electrode can enhance the resistance switching behavior of α-In_2Se_3 ferroelectric memristors. Our method offers an efficient and universal approach for transferring metals with varying adhesion forces and complex patterns, which is significant not only for fabricating high-performance 2D semiconductor devices but also for constructing complex microstructures.

Acknowledgments

This work was supported by the National Key Research & Development Project of China (Grant No. 2022YFA1204100), the National Natural Science Foundation of China (Grant No. 62488201), Strategic Priority Research Program of Chinese Academy of Sciences (CAS, Grant Nos. XDB30000000 and XDB28000000), CAS Project for Young Scientists in Basic Research (Grant No. YSBR-003), the Innovation Program of Quantum Science and Technology (Grant No. 2021ZD0302700), and Beijing Outstanding Young Scientist Program (Grant No. BJJWZYJH01201914430039). This research benefited from resources and support from the Electron Microscopy Center at the University of Chinese Academy of Sciences.

References

[1] Nikonov D E and Young I A 2015 *IEEE J. Explor. Solid-State Comput. Devices Circuits* **1** 3
[2] Li W, Shen H, Qiu H, Shi Y and Wang X 2024 *Natl. Sci. Rev.* **11** nwae001
[3] O'Brien K P, Naylor C H, Dorow C, Maxey K, Penumatcha A V, Vyatskikh A, Zhong T, Kitamura A, Lee S, Rogan C, Mortelmans W, Kavrik M S, Steinhardt R, Buragohain P, Dutta S, Tronic T, Clendenning S, Fischer P, Putna E S, Radosavljevic M, Metz M and Avci U 2023 *Nat. Commun.* **14** 6400
[4] Zeng S, Liu C and Zhou P 2024 *Nat. Rev. Electr. Eng.* **1** 335
[5] Radisavljevic B, Radenovic A, Brivio J, Giacometti V and Kis A 2011 *Nat. Nanotechnol.* **6** 147
[6] Jiang J, Xu L, Qiu C and Peng L M 2023 *Nature* **616** 470
[7] Wu L, Wang A, Shi J, Yan J, Zhou Z, Bian C, Ma J, Ma R, Liu H, Chen J, Huang Y, Zhou W, Bao L, Ouyang M, Pennycook S J, Pantelides S T and Gao H J 2021 *Nat. Nanotechnol.* **16** 882
[8] Wang H, Guo H, Guzman R, JiaziLa N, Wu K, Wang A, Liu X, Liu L, Wu L, Chen J, Huan Q, Zhou W, Yang H, Pantelides S T, Bao L and Gao H J 2024 *Adv. Mater.* **36** 2311652
[9] Wang H, Bao L, Guzman R, Wu K, Wang A, Liu L, Wu L, Chen J, Huan Q, Zhou W, Pantelides S T and Gao H J 2023 *Adv. Mater.* **35** 2301067
[10] Migliato Marega G, Zhao Y, Avsar A, Wang Z, Tripathi M, Radenovic A and Kis A 2020 *Nature* **587** 72
[11] Siyuan W, Li Y, Li W, Mao X, Wang C, Chen C, Dong J, Nie A, Xiang J, Liu Z, Zhu W and Zeng H 2019 *Adv. Funct. Mater.* **29** 1808606
[12] Zheng C, Yu L, Zhu L, Collins J L, Kim D, Lou Y, Xu C, Li M, Wei Z, Zhang Y, Edmonds M T, Li S, Seidel J, Zhu Y, Liu J Z, Tang W X and Fuhrer M S 2018 *Sci. Adv.* **4** eaar7720
[13] Zhou Y, Wu D, Zhu Y, Cho Y, He Q, Yang X, Herrera K, Chu Z, Han Y, Downer M C, Peng H and Lai K 2017 *Nano Lett.* **17** 5508
[14] Xue F, He X, Retamal J R D, Han A, Zhang J, Liu Z, Huang J K, Hu W, Tung V, He J H, Li L J and Zhang X 2019 *Adv. Mater.* **31** 1901300
[15] Liu K, Zhang T, Dang B, Bao L, Xu L, Cheng C, Yang Z, Huang R and Yang Y 2022 *Nat. Electron.* **5** 761
[16] Si M, Zhang Z, Chang S C, Haratipour N, Zheng D, Li J, Avci U E and Ye P D 2021 *ACS Nano* **15** 5689
[17] Sun Y, Wang S, Chen X, Zhang Z and Zhou P 2022 *Adv. Intell. Syst.* **4** 2100198
[18] Xue F, He X, Wang Z, Retamal J R D, Chai Z, Jing L, Zhang C, Fang H, Chai Y, Jiang T, Zhang W, Alshareef H N, Ji Z, Li L J, He J H and Zhang X 2021 *Adv. Mater.* **33** 2008709
[19] Schulman D S, Arnold A J and Das S 2018 *Chem. Soc. Rev.* **47** 3037
[20] Ghani M A, Sarkar S, Lee J I, Zhu Y, Yan H, Wang Y and Chhowalla M 2024 *ACS Appl. Mater. Interfaces* **16** 7399
[21] Allain A, Kang J, Banerjee K and Kis A 2015 *Nat. Mater.* **14** 1195
[22] Liu Y, Guo J, Zhu E, Liao L, Lee S J, Ding M, Shakir I, Gambin V, Huang Y and Duan X 2018 *Nature* **557** 696
[23] Zhang X, Huang C, Li Z, Fu J, Tian J, Ouyang Z, Yang Y, Shao X, Han Y, Qiao Z and Zeng H 2024 *Nat. Commun.* **15** 4619
[24] Jung Y, Choi M S, Nipane A, Borah A, Kim B, Zangiabadi A, Taniguchi T, Watanabe K, Yoo W J, Hone J and Teherani J T 2019 *Nat. Electron.* **2** 187
[25] Fang H, Chuang S, Chang T C, Takei K, Takahashi T and Javey A 2012 *Nano Lett.* **12** 3788
[26] Kappera R, Voiry D, Yalcin S E, Branch B, Gupta G, Mohite A D and Chhowalla M 2014 *Nat. Mater.* **13** 1128
[27] Yu J, Wang H, Zhuge F, Chen Z, Hu M, Xu X, He Y, Ma Y, Miao X and Zhai T 2023 *Nat. Commun.* **14** 5662
[28] Shen P C, Su C, Lin Y, Chou A S, Cheng C C, Park J H, Chiu M H, Lu A Y, Tang H L, Tavakoli M M, Pitner G, Ji X, Cai Z, Mao N, Wang J, Tung V, Li J, Bokor J, Zettl A, Wu C I, Palacios T, Li L J and Kong J 2021 *Nature* **593** 211
[29] Li W, Gong X, Yu Z, Ma L, Sun W, Gao S, Koroglu C, Wang W, Liu L, Li T, Ning H, Fan D, Xu Y, Tu X, Xu T, Sun L, Wang W, Lu J, Ni Z, Li J, Duan X, Wang P, Nie Y, Qiu H, Shi Y, Pop E, Wang J and Wang X 2023 *Nature* **613** 274
[30] Liu G, Tian Z, Yang Z, Xue Z, Zhang M, Hu X, Wang Y, Yang Y, Chu P K, Mei Y, Liao L, Hu W and Di Z 2022 *Nat. Electron.* **5** 275
[31] Wu Y, Xin Z, Zhang Z, Wang B, Peng R, Wang E, Shi R, Liu Y, Guo J, Liu K and Liu K 2023 *Adv. Mater.* **35** 2210735
[32] Qi D, Li P, Ou H, Wu D, Lian W, Wang Z, Ouyang F, Chai Y and Zhang W 2023 *Adv. Funct. Mater.* **33** 2301704
[33] Hu S, Luo X, Xu J, Zhao Q, Cheng Y, Wang T, Jie W, Castellanos-Gomez A, Gan X and Zhao J 2022 *Adv. Electron. Mater.* **8** 2101176
[34] Hong M, Zhang X, Geng Y, Wang Y, Wei X, Gao L, Yu H, Cao Z, Zhang Z and Zhang Y 2023 *InfoMat* **6** e12491
[35] Liang Q, Luo X Y, Wang Y X, Liang Y C and Xie Q 2022 *Chin. Phys. B* **31** 087101
[36] Ma L, Wang Y and Liu Y 2024 *Chem. Rev.* **124** 2583
[37] Wu L, Shi J, Zhou Z, Yan J, Wang A, Bian C, Ma J, Ma R, Liu H, Chen J, Huang Y, Zhou W, Bao L, Ouyang M, Pantelides S T and Gao H J 2020 *Nano Res.* **13** 1127
[38] Ryou J, Kim Y S, Kc S and Cho K 2016 *Sci. Rep.* **6** 29184
[39] Qin B, Ma C, Guo Q, Li X, Wei W, Ma C, Wang Q, Liu F, Zhao M, Xue G, Qi J, Wu M, Hong H, Du L, Zhao Q, Gao P, Wang X, Wang E, Zhang G, Liu C and Liu K 2024 *Science* **385** 99
[40] Pasquale G, Lopriore E, Sun Z, Cernevics K, Tagarelli F, Watanabe K, Taniguchi T, Yazyev O V and Kis A 2023 *Nat. Nanotechnol.* **18** 1416
[41] Zhang Y, Chen X, Zhang M, Wu X, Wang J, Tian R, Fang L, Zhang Y, Zhao J and Gan X 2024 *Adv. Funct. Mater.* **34** 2402957
[42] Chen Y, Zhang M, Li D, Tang Y, Ren H, Li J, Liang K, Wang Y, Wen L, Li W, Kong W, Liu S, Wang H, Wang D and Zhu B 2023 *ACS Nano* **17** 12499
[43] Zhang Y, Wang L, Chen H, Ma T, Lu X and Loh K P 2021 *Advanced Electronic Materials* **7** 2100609
[44] Xue F, He X, Ma Y, Zheng D, Zhang C, Li L J, He J H, Yu B and Zhang X 2021 *Nat. Commun.* **12** 7291
[45] Zhou J, Fei P, Gu Y, Mai W, Gao Y, Yang R, Bao G and Wang Z L 2008 *Nano Lett.* **8** 3973